Int. J. Electrochem. Sci., 11 **(2016)** 4267 – 4282, doi: 10.20964/2016.06.60

International Journal of ELECTROCHEMICAL SCIENCE
www.electrochemsci.org

The Study of Supercapacitive Stability of MnO_2/MWCNT Nanocomposite Electrodes by Fast Fourier Transformation Continues Cyclic Voltammetry

Hamid Reza Naderi[1], *Mohammad Reza Ganjali*[1,2] *and Parviz Norouzi*[1,2,*]

[1]Center of Excellence in Electrochemistry, Faculty of Chemistry, University of Tehran, Tehran, Iran
[2]Biosensor Research Center, Endocrinology & Metabolism Molecular-Cellular Sciences Institute, Tehran University of Medical Sciences, Tehran, Iran
[*]E-mail: norouzi@khayam.ut.ac.ir

Received: 14 March 2016 / *Accepted:* 7 April 2016 / *Published:* 4 May 2016

In this work, the nanostructured MnO_2 was uniformly coated on the multi-walled carbon nanotube (MWCNT) by a sonochemical method, and the effect of MWCNT amount on the supercapacitive performance of the nanocomposites were investigated. The structure and morphology of the nanocomposites were characterized by X-ray diffraction (XRD), thermogravimetric analysis (TGA), transition electron microscopy (TEM) and scanning electron microscopy (SEM). Also, the specific capacitances (SCs) of the MWCNT/MnO_2 electrodes were studied by cyclic voltammetry (CV). The result shows that the loading the nanocomposite with of MnO_2 was 65 wt. %, the electrode has a high SC of 394 F g^{-1} (at scan rate of 2 mV s^{-1} in a 0.5 M Na_2SO_4) indicating a better performance than that of pristine MnO_2 electrodes (289 F g^{-1} at scan rate of 2 mV s^{-1}). Fast Fourier transformation continuous cyclic voltammetry (FFTCCV) technique was used to study stability and separation of charge and discharge curves of the nanocomposite electrodes, over a large number of cycles (at scan rates 200 mV s^{-1}). The results indicated SC that the capacitance of the composite electrode decreases only 3.2% of initial capacitance, after 4000 cycles. Therefore, the prepared composite could be potential electrode materials for supercapacitors.

Keywords: Supercapacitors, Continuous cyclic voltammetry, nanocomposite, MnO_2 nanostructures, Carbon nanotube, Sonochemistry

1. INTRODUCTION

Supercapacitors are considered as the applicable energy-storage devices, which are used for various electrical systems, such as mobile devices and hybrid electric vehicles [1]. In fact, they have higher power density and longer cycle life than batteries while energy density is lower than batteries.

The charge storage mechanism of a Supercapacitor combines non-faradic charge (double layer capacitance) and faradaic reactions [2]. On the basic, these two mechanism supercapacitors are classified as: electric double-layer capacitors (EDLCs) that employ typical form carbons and pseudocapacitors that employ transition metal oxide compounds (e.g. RuO_2, NiO, MnO_2, Co_2O_3, IrO_2, FeO, SnO_2, V_2O_5) or conducting polymers (polyaniline, polypyrrole) [3-14].

In recent years, supercapacitors based on MnO_2 as electroactive materials are attracting great attention due to the low cost of the raw material, excellent electrochemical performance and environmental compatibility [15-27]. The pseudocapacitance in MnO_2 was explained by two reaction mechanisms proposed for the charge storage in MnO_2 based electrodes. The first mechanism is based on the concept of intercalation/ deinteracalation of protons (H^+) or alkali metal cations such as Na^+, K^+ in the bulk of the material during redox reaction, that described by the following reaction [16, 18].

$$MnO_2 + M^+ + e \underset{discharge}{\overset{charge}{\rightleftarrows}} MnOOM \qquad (1)$$

Where $M^+ = H^+, Na^+, K^+, Li^+$.

The second mechanism involves the surface adsorption/ desorption of alkali metal cations (M^+) on MnO_2 [16].

$$(MnO_2)_{surface} + M^+ + e \underset{discharge}{\overset{charge}{\rightleftarrows}} (MnOOM)_{surface} \qquad (2)$$

The main difference between the two mechanisms is the difference in the corresponded reacting sites. The majority of “bulk” Mn sites are involved in the intercalation/deinteracalation mechanism while the surface Mn sites have priority in the reaction based on the adsorption/desorption mechanism [19]. Toupin et al. using X-ray photoelectron spectroscopy confirmed that the amorphous or poorly crystalline MnO_2 shows the adsorption/desorption mechanism [17]. Also, Kuo et al. by in situ synchrotron X-ray diffraction analysis demonstrated that the intercalation/ deinteracalation process occurs mostly on the crystalline MnO_2 compounds [18]. But high relative resistance of MnO_2 reduces charge storage, thus its commercial use is limited [20-22].

In order to improve the conductivity of MnO_2, conductive fillers, such as exfoliated graphite [23, 24], graphite nanoplatelet [25], reduced graphene oxide [26] mesoporous carbons [27, 28] carbon black [29] and carbon nanotubes (CNT) [30-36] and other conducting materials are usually composited with MnO_2. Recently, many researchers in supercapacitors have focused on the MnO_2/CNT composites because CNT has excellent electronic conductivity, available specific surface area and high chemical stability [37, 38].

In this work, the synthesis of the MnO_2/MWCNT nanocomposites with various mass MWCNT to MnO_2 ratios by sonochemical method is reported. These nanocomposites were characterized by XRD, TGA, SEM and TEM. Also, supercapacitive properties of the MnO_2 and MnO_2/MWCNT electrodes with various ratios were examined by cyclic voltammetry (CV), FFT Continuous cyclic voltammetry (FFTCCV), galvanostatic charge/discharge, and electrochemical impedance spectroscopy (EIS). The supercapacitive properties of the electrodes were studied by FFTCCV technique over a large number of cycles at high scan rates [39, 40]. This technique provided specific information about the changes in charge exchange in the anodic and cathodic section of the CVs [41-47]. Electrochemical characterizations indicated that the SC of nanocomposite electrodes shows enhanced capacitance compared to that of pure MnO_2 electrode.

2. EXPERIMENTAL

2.1. Preparation of MnO_2/MWCNT nanocomposites

For introducing surface functional groups and remove the catalyst particles and other impurities, MWCNTs (Shenzhen Nanotech Port) were refluxed in 15 wt. % nitric acid at boiling temperature for 6.0 h. Predetermined amounts of MWCNT (25, 35 and 45 wt. %) were added to the aqueous solutions of 0.25 M $MnSO_4$ (Merck, research grade) and 0.5 M $KBrO_3$ (Merck, research grade) with the total volume of 100 mL. The mixture was irradiated with ultrasound radiation with 480 W cm^{-2} input power and working frequency of 24 kHz. A titanium horn transducer system (UP 200 H, Dr. Hielscher GmbH) with a 2 mm microtip was employed. The titanium horn was inserted to a depth of 2 cm into the solution (51-55 °C).

2.2. Structure characterization

Crystal phases of the MWCNT, MnO_2 and MnO_2/MWCNT nanocomposites were identified by an X-ray diffractometer (Bruker, D8-advance) at 2θ=4-70° with monochromatized Cu Kα radiation (λ=1.541874 Å) operated at 40 kV/30 mA. TGA for samples were recorded in the temperature range from 20 °C to 900 °C in air atmosphere at a heating rate of 10 °C per min using TG 209 F1 (Netzsch) tester. The morphologies of the samples were observed by SEM (Philips, XL30) and TEM (Ziess, EM900 and 80 Kev). To imaging the nanocomposite using TEM, a suspension of the prepared sample in ethanol was drop-casted onto carbon-coated copper grids and dried.

2.3. Electrochemical Measurement

Working electrodes were prepared by mixing of the MnO_2/MWCNT nanocomposite as active material 5 wt. % of polytetrafluoroethylene (PTFE) dried powder (Merck) that PTFE was used as the binder. Then, a few drops of ethanol, added to the mixture to make a supplementary homogeneous solution. Subsequently, the mixture was coated onto the steel grid substrate (0.7 cm^2) with a spatula, and then pressed at 15 MP.

CV, CP and EIS measurements were performed using a potentiostat/galvanostat (PGSTAT30, Autolab, Echo Chemie) in a three-electrode glass cell. The steel-mesh was coated with MnO_2/MWCNT nanocomposites as the working electrode, Platinum foil as the counter and Ag/AgCl electrode (Metrohm AG 9101 Herisau, 3 M KCl, 0.207 V versus, SHE at 25 °C) as the reference electrode. The measurements were carried out in a 0.5 M Na_2SO_4 aqueous electrolyte at pH 3.3. The solution temperature was maintained at 25 °C by a water thermostat.

2.4. FFTCCV technique

The experimental data collection was performed with the help of the following equipment; a setup of a computer, equipped with a data-acquisition board (PCL-818HG, Advantech Co.) and a custom-made potentiostat described in our previous works [39-47]. A computer program was developed in Delphi6® environment that was used for data acquisition and processing.

3. RESULTS AND DISCUSSION

3.1. Structure characterization

The XRD patterns for MnO_2, MWCNT and MnO_2/MWCNT nanocomposites with several ratios are shown in Fig. 1. As shown in the figure, the diffraction peaks at 2θ=21.63°, 37.19°, 38.71°, 41.9°, 42.42°, 55.56°, 66.67° and 68.20° can be readily indexed as the pure orthorhombic γ-MnO_2 crystal planes of the (1 2 0), (2 3 0), (3 0 0), (0 0 2), (1 6 0), (2 4 2), (4 2 1) and (0 0 3), respectively, (JCPDS card no. 14–644) [27]. The crystalline structure of MnO_2 are composed of one Mn atom surrounded by six O atoms to form an octahedron. The MnO_6 octahedral subunits share vertices and edges to form crystalline tunnel structures by continuously linking to the neighboring subunits. The structure of γ-MnO_2 is widely accepted as a random intergrowth of 1×1 tunnels of pyrolusite and 1×2 tunnels of ramsdellite [48, 49]. According to Fig. 1, the XRD pattern of the MWCNT shows a peak at 2θ=25.77° corresponding to the (0 0 2) and with the increasing of MWCNT portion in composite, the intensity of this peak was increased.

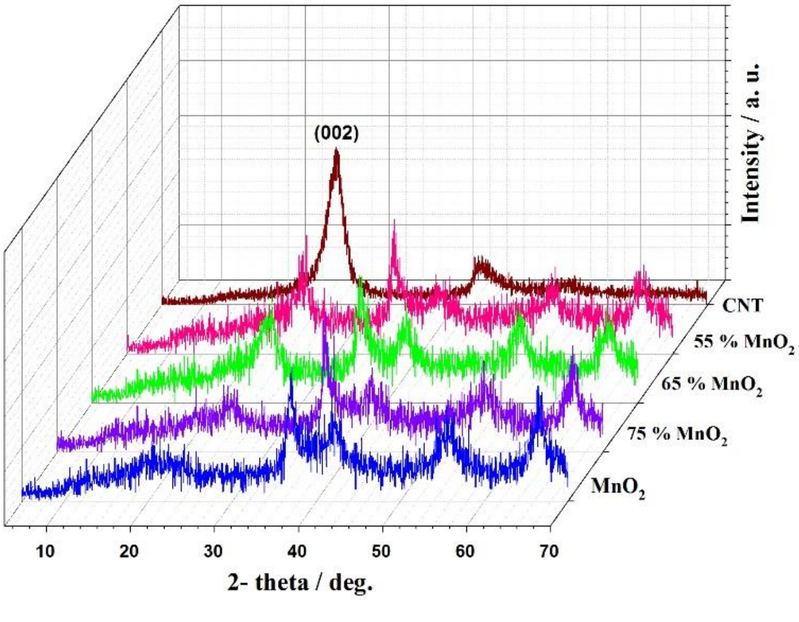

Figure 1. X-ray diffraction patterns of MWCNT, pure γ-MnO_2 and MnO_2/MWCNT nanocomposites with various mass ratios

TGA thermograms of γ-MnO_2 and MnO_2/MWCNT nanocomposite powders are shown in Fig. 2. TGA was employed to determine the actual content of each component in samples. Four variations of the TGA thermogram of γ-MnO_2 powders are shown in the temperature range of 20-150, 150-500, 500-550 and 850-900 °C. The first weight change at 20-100 °C related to dehydration of the γ-MnO_2 powders. The second weight loss in the range of 150-500 °C could be related to the water molecule removing from the γ-MnO_2 crystallization powder (which is shown in the molecular formula). However, the small weight loss in the ranges of 500-550 °C and 850-900 °C were observed in the TGA thermogram, could be associated to the omitting the oxygen from manganese oxide lattice, due to the phase transition, MnO_2 to Mn_2O_3, and the transition Mn_2O_3 to Mn_3O_4 [29, 50].

From TGA thermograms of the nanocomposite powder could be estimated content of MWCNT. It was found that the weight percent of MWCNT in the nanocomposite was about 35 wt. %. TGA thermogram for the nanocomposite containing 65% MnO_2/MWCNT, shows a slight decrease (6 wt. %) at temperatures up to 200 °C, which could be corresponded to dehydration of crystalline or the physically adsorbed water. A sharp weight loss in the range of 400–600°C and the 35wt. % loss observed in the TGA data is related to the combustion of MWCNT from the nanocomposite.

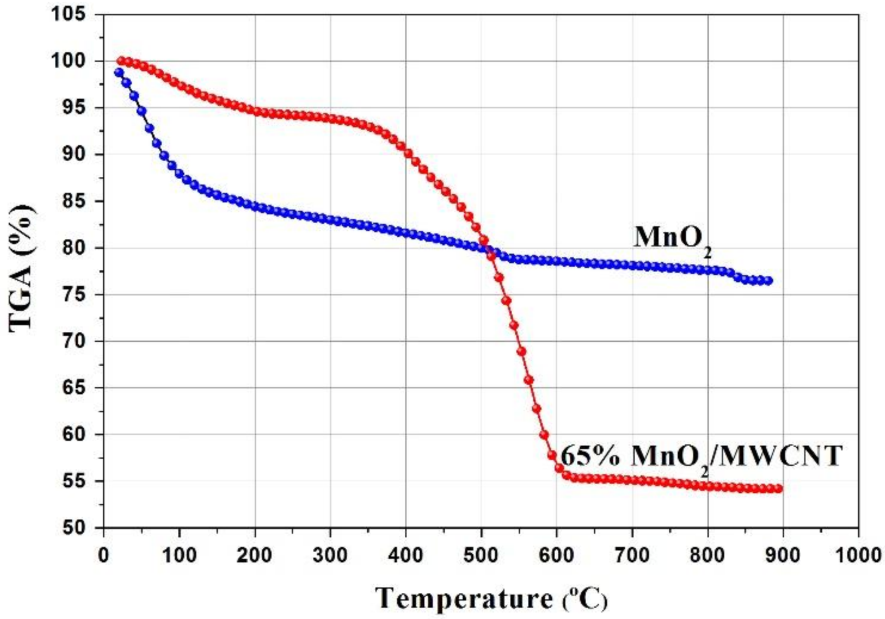

Figure 2. TGA thermograms of MnO_2 and 65% MnO_2/MWCNT nanocomposites

3.2. Morphology characterization

Fig. 3 shows SEM images of the pure MnO_2 (a), and MnO_2/MWCNT nanocomposite (b and c), respectively. In Fig. 3a, the MnO_2 nanoparticles, in addition to their aggregation, they have almost a spherical shape with diameters of in rage of 30-60 nm. For the new nanocomposite, as shown in Fig. 3c the particle size of MnO_2 was estimated to be range of 20 to 50 nm. Furthermore, Fig. 3b and 3c shows that MnO_2 are distributed uniformly onto MWCNTs surface. Fig. 3d shows a TEM image of the MnO_2/MWCNT nanocomposite. The figure, also, conforms the SEM results in which the MnO_2 nanoparticles are spread in the MWCNTs matrix.

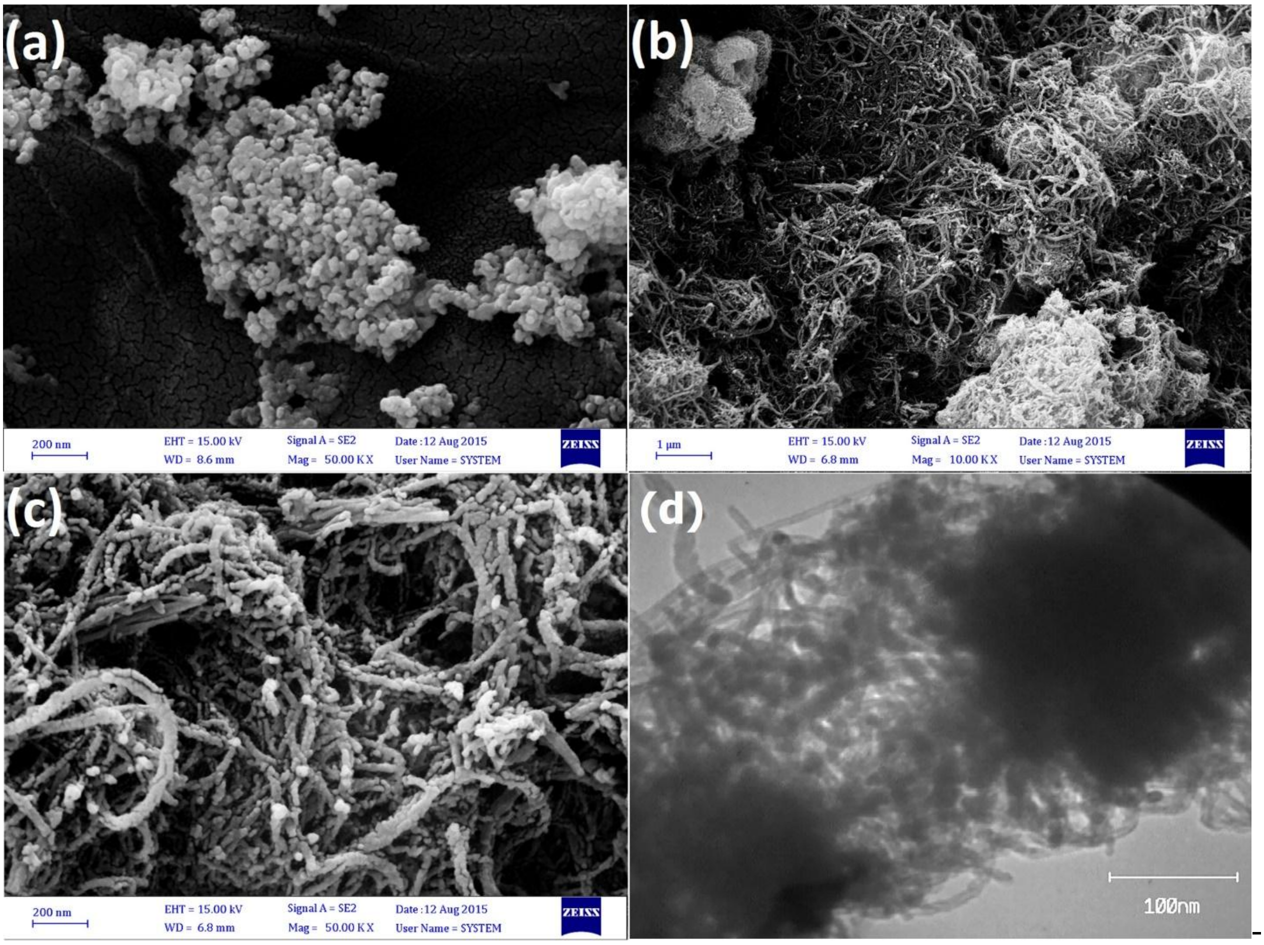

Figure 3. SEM images of MnO_2 (a), MnO_2/MWCNT nanocomposite (b, c) and TEM images of MnO_2/MWCNT nanocomposite (d)

3.3. Electrochemical characterization

3.3.1. CV and specific capacitances

The electrochemical performance of the MnO_2 and MnO_2/MWCNT electrodes were evaluated by CV, and the results are shown in Fig. 4. The SCs of the electrodes can be calculated from CV according to the following equation [1]:

$$SC = \frac{1}{v\Delta V}\int_{V_i}^{V_f} i\,dV \qquad (3)$$

Where dV is voltage difference, the v is the scan rate (V s^{-1}), the V_i is the initial voltage (V), the V_f is the final voltage. Fig. 4a shows the CVs, in a potential rang of 0.0 to 1.0 V, for pure MnO_2 and 65% MnO_2/MWCNT electrodes in 0.5 M Na_2SO_4 electrolyte, at a scan rate of 50 mVs^{-1}. Both CVs shows approximate mirror images, respect to the zero-current line. In fact, observing a rapid current response to voltage reversal at the end of each potential indicates the ideal pseudocapacitive behavior of the constructed nanocomposite electrodes. The SCs values of pure MnO_2 and 65% MnO_2/MWCNT electrodes were 181 F g^{-1} and 292 F g^{-1} at the scan rate of 50 mV s^{-1}, respectively. The obtained SCs of the 65% MnO_2/MWCNT electrode is 65% higher than SCs of the pure MnO_2 electrode. Such enhancement in SCs can be attributed to the synergy effects of each pristine component in the nanocomposites. Also, part of the enhancement in SCs, could be due to the existence of smaller particle size on the electrode surface, which provided a high specific surface area. This could cause an increase the number of available active sites and thus boost the amount of energy that may store in the supercapacitor electrodes [24]. Fig. 4b illustrations the CV curves of MnO_2/MWCNT electrode with various mass ratios. The area of the CV loop of 65% MnO_2/MWCNT electrode, is significantly larger than that of the other MnO_2/MWCNT electrodes.

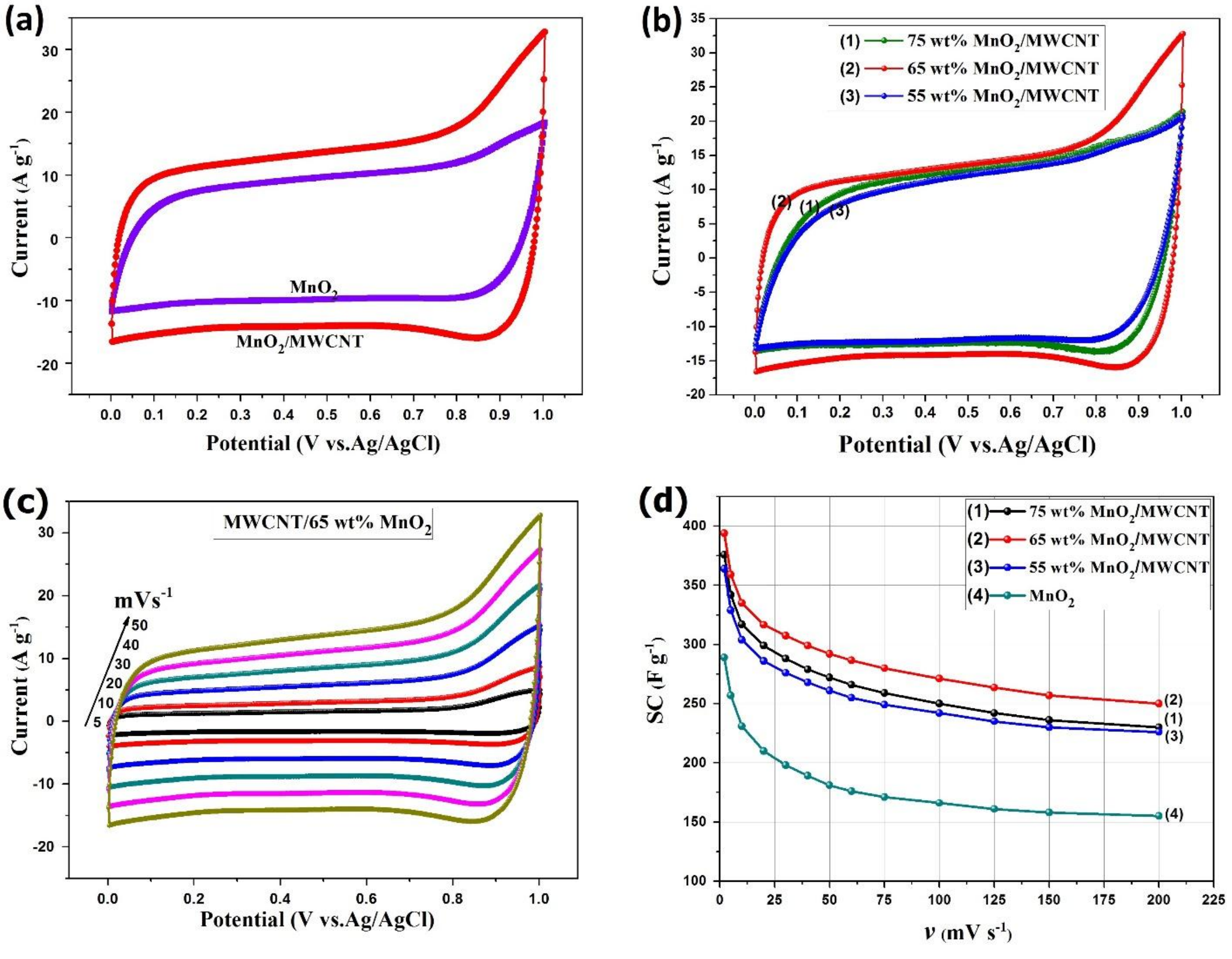

Figure 4. The CVs of MnO_2 and 65% MnO_2/MWCNT electrode at a scan rate of 50 mV s^{-1} (a), CVs of MnO_2/MWCNT electrodes with various mass ratios at a scan rate of 50 mV s^{-1} (b), and CVs of 65% MnO_2/MWCNT electrode at various scan rates (c), and the SC of MnO_2 and MnO_2/MWCNT electrodes with different ratios at different scan rates (d)

Fig. 4c shows the CVs of the pure 65% MnO_2/MWCNT electrodes at various scan rates (5-50 mV s^{-1}). These curves are quasi-rectangular showing ideal pseudocapacitance behavior and fast charging/discharging process characteristic. However, the distance between levels anodic and cathodic currents at the same scan rates is much smaller than obtained for 65% MnO_2/MWCNT electrode, which indicates a lesser SCs. The change in SCs as a function of the scan rates for the MnO_2 electrode and MnO_2/MWCNT electrode are plotted in Fig. 4d. As shown SCs for 65% MnO_2/MWCNT decrease from 394 to 250 F g^{-1} with scan rate, from 2 to 200 mV s^{-1}. Based on these results, one could be suggested that at low scan rates; the electrolyte ions (Na^+ or H^+) inserted into the available pores of the MnO_2 structure. This could lead to procurement a higher effective the redox reaction and a high capacitance. But when the scan rate is increased to 200 mV s^{-1} or higher, the effective interaction between the electrolyte ion and the pores is significantly decreased. In this condition, effective redox reaction occurred only to the outer surface of the electrode, which caused a decline in the total capacitance.

Also, In the Fig. 4d demonstrates the change in SCs with the change of MWCNT in the nanocomposite electrodes. The percentage of MWCNT content in the nanocomposite had a direct effect the nanocomposite conductivity, where any decrease in MWCNT resulted in a decrease in the capacitance of the electrodes. In fact, the amount of MWCNT in the nanocomposite reaches 35% the conductivity of the nanocomposite enhanced. However, when amount of MWCNT goes to more than 35%, the faradic capacitance decreased, but the double layer capacitance increased. Still, the value of the double layer capacitance enhancement was much smaller than the value decline in the faradic capacitance.

3.3.2. FFTCCV measurements

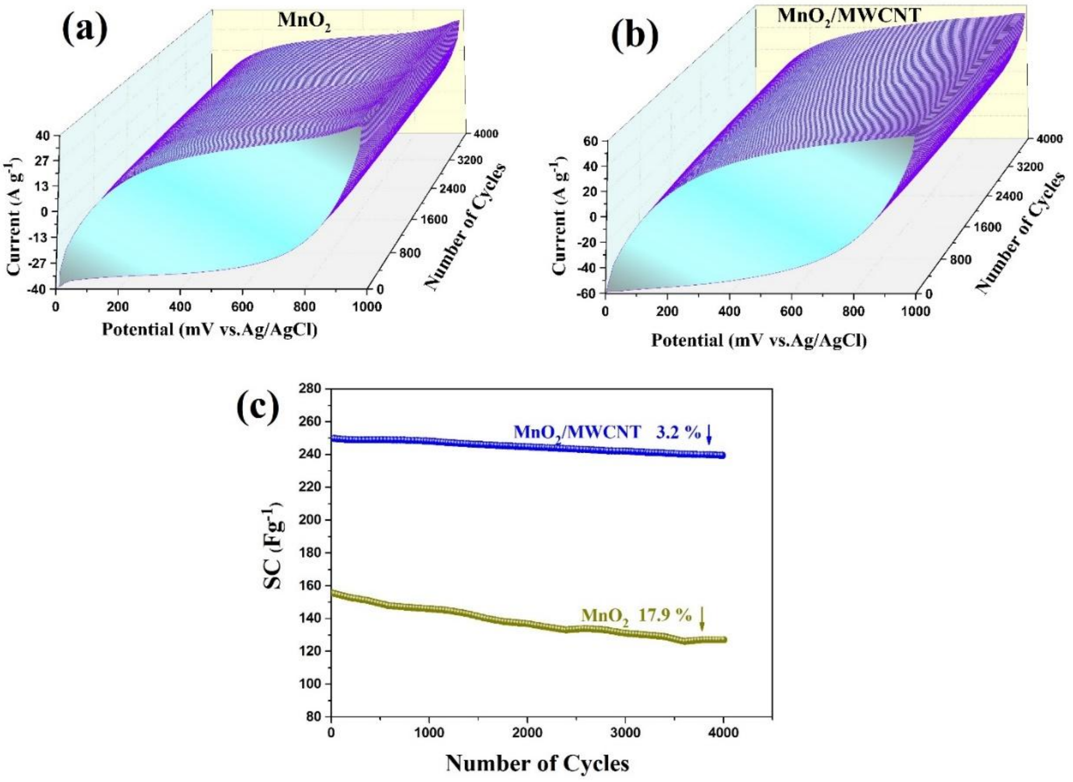

Figure 5. The MnO_2 and 65% MnO_2/MWCNT electrode 3D-FFTCCV curves as a function of time at measured 200 mV s^{-1} (a, b). Variation of the SC of MnO_2 and 65% MnO_2/MWCNT electrode as a function of number of cycles at measured 200 mV s^{-1} (c)

The FFCCV technique could be considered the best tools for examination of variation charge storage of a supercapacitor during that potential cycling [45-47]. In this method, under a long-term potential cycling, the stability of the electrodes is evaluated. Fig. 5a and Fig. 5b show three-dimensional (3D) FFTCCVs of MnO_2 and 65% MnO_2/MWCNT electrode, which was performed at a scan rate of 200 mV s^{-1} in 0.5 M Na_2SO_4, respectively.

In these two 3D-plots, the changes in the CVs over number of cycles are more noticeable. As shown in Fig. 5c, the SC of MnO_2 electrode retain at 82.1% of its original value, at scan rate 200 mVs^{-1} for 4000 cycles in 0.5 M Na_2SO_4. Also, shows changes the value SC of the 65% MnO_2/MWCNT electrode, where it decreases slightly at the beginning and then, decreases only 3.2%, after applying 4000 CVs. In the other measurements, after applying 4000 CVs. The above results prove that the 65% MnO_2/MWCNT electrode are highly stable during potential cycling test compared to MnO_2 electrode.

Fig. 6a and 6b illustrates the absolute capacitive charge changes in the CVs curves in during time. In fact, the details of the occurring changes can even be seen well, when the current at recorded CVs subtracted from the current at background (or reference) CV, where the reference CV was obtained by averaging 5 CVs at the beginning of the measurement. As seen in Fig. 6a and 6b current in the central potential no significant changes, but further current changes can be observed in the initial potential and the final potential.

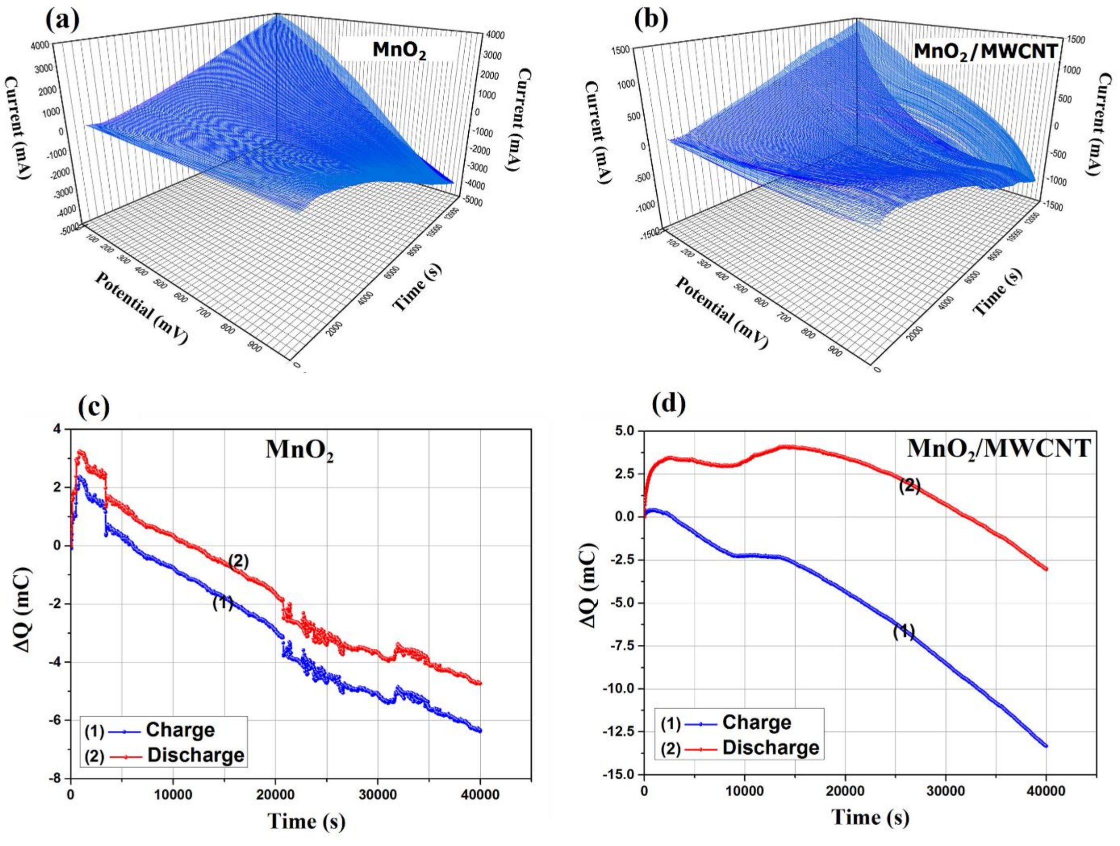

Figure 6. Curves result from the subtraction of 5 CVs average background from the subsequent CVs at measured 200 mV s^{-1} for MnO_2 electrode (a) and 65% MnO_2/MWCNT electrode (b), Variation of the capacitive current of the charge and discharge curves separately as a function of time for MnO_2 electrode (c) and 65% MnO_2/MWCNT electrode (d).

Another advantage of FFTCCV technique is investigated separately charge and discharge behavior of the electrodes. Fig. 6c and 6d is compared the charging and discharging behavior of MnO_2 and 65% MnO_2/MWCNT electrode at a scan rate of 200 mV s^{-1}. As shown in Fig. 6c, the change in capacitance during charge and discharge of MnO_2 electrode, where the curves are almost identical and symmetrical. This may due to the same resistance for entering and exiting of the cations in the pores of the MnO_2 nanoparticles. Fig .6d shows the charge and discharge behavior of 65% MnO_2/MWCNT electrode. As shown in the figure, curves for capacitance changes during the charge and discharge are not symmetrical. As demonstrated in the figures, the capacitance changes in the charge curve is greater than the discharge curve. This behavior could be concluded that easily cations entering into the pores. But, in discharge, those cations could be hardly exited from the pores. Likewise, in Fig. 6d, the difference in capacitance reduction is observed between the two curves at the beginning of the curve (until to 10000 s). After this time, the difference in capacitance reduction is equal. This behavior indicates that pores over time be modified and resistance to entry and exit of cations in is equal in the pores.

3.4. Galvanostatic charge/discharge

The galvanostatic charge/discharge analysis can be consider as a dependable technique, for evaluation the supercapacitive performance of the electrodes under controlled conditions. We used a three-electrode system and applied a potential window of 0.0 to 1.0 V (vs. Ag/AgCl) to provide complementary measurements.

Fig. 7a shows the charge/discharge curves of the MnO_2/MWCNT electrodes at different current densities, ranging from 2 to 24 A g^{-1}. As can be seen, the curves' shapes are triangular, linear, symmetric and very sharp. The equal durations of charging and discharging for each electrode imply a reversible behavior, a high columbic efficiency, and an ideal capacitor performance. Also, in the case of 65% MnO_2/MWCNT electrode, there is a lesser of a decrement in the value of SC with increasing current density compare with the measured SC for other electrodes. Fig. 7b shows the charge/discharge curves of MnO_2/MWCNT electrodes with different ratios at a current density of 2.0 Ag^{-1} in 0.5 M Na_2SO_4. Equilateral triangle shapes for MnO_2/MWCNT electrodes suggest an ideal capacitive behavior and a good reversibility during the charge/discharge processes. This could be attributed to the capacitive behavior via the following features: 1) the valuable electrical conductivity of MWCNT caused a reduction in the internal resistance of MnO_2 nanoparticles, 2) fast redox reactions due to facilitated charge transport from MnO_2 as a function of uniform distribution of MnO_2 nanoparticles on the MWCNT. The SCs values were calculated from charge/discharge cycles using the following equation:

$$SC = \frac{I\Delta t}{\Delta V} \qquad (4)$$

Where SC is the specific capacitance based on the mass of the electroactive material (F g^{-1}), ΔV is the potential window of discharge (V), and Δt is the discharge time (s). The 65% MnO_2/MWCNT electrode shows the largest value of SC, 294 Fg^{-1} when the current density is 2 Ag^{-1}. These results are indication of existing of a higher accessible active sites in the 65% MnO_2/MWCNT electrode compare with the other electrodes with different ratios. Also, the value of SC data obtained from charge/discharge for the electrodes are in good agreement with the obtained SC from CV measurements.

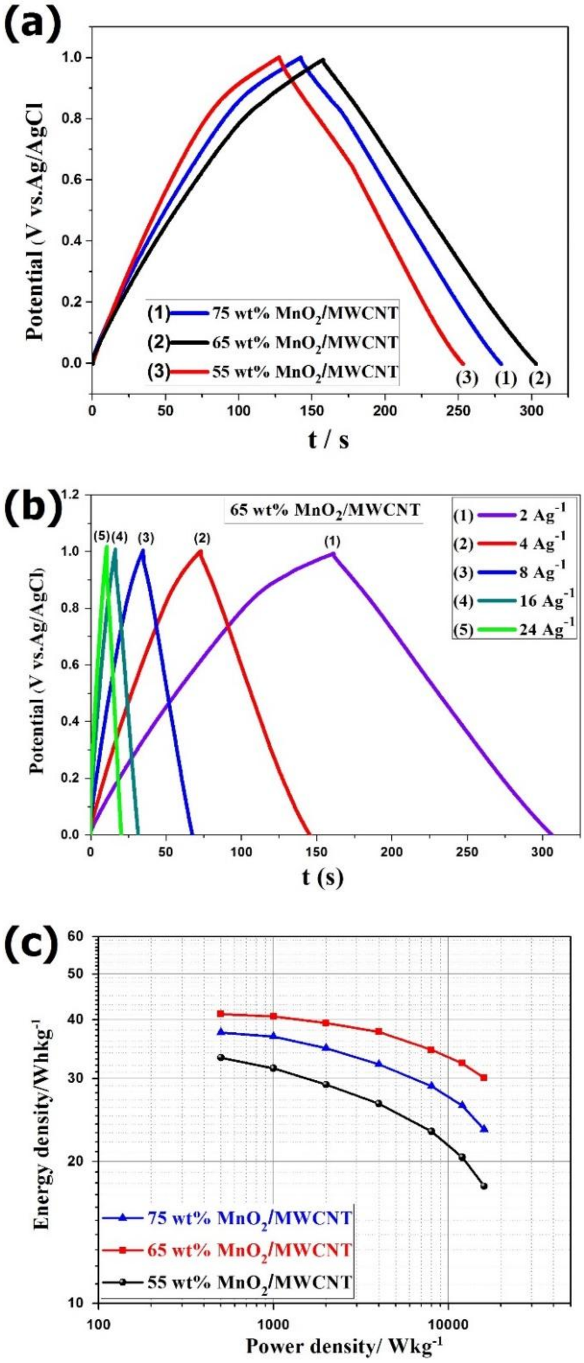

Figure 7. Charge/discharge curves of the 65% MnO_2/MWCNT electrode at different current densities (a), Charge/discharge curves of 65% MnO_2/MWCNT electrode with different ratios at a current density of 2.0 A g^{-1} (b) and the Ragone plots obtained for MnO_2/MWCNT electrodes with different ratios (c).

Ragone plots depict the relationship of power densities and energy densities. Fig. 7c shows the Ragone plots of the 65% MnO_2/MWCNT electrodes with different ratios. The energy and power densities were derived from charge/discharge curves at various current densities. The energy density (E_d) and power density (P_d) of a supercapacitor cell in the Ragone plots were calculated using the equations of:

$$E_d = \frac{1}{2} C (\Delta V)^2 \qquad (5)$$

and

$$P_d = \frac{E_d}{t} \qquad (6)$$

Where P_d and E_d are the power density (W kg^{-1}) and energy density (W h kg^{-1}), respectively. C is the specific capacitance based on the mass of the electroactive material (F g^{-1}), ΔV is the potential window of discharge (V), and t is the discharge time (s). The 65% MnO_2/MWCNT electrodes shows significant enhancement in both the E_d and the P_d. The 65% MnO_2/MWCNT electrode shows E_d and the P_d better than other nanocomposite electrodes. The 65% MnO_2/MWCNT electrode shows E_d of 41.1 W h kg^{-1} at the P_d of 500 W kg^{-1} and P_d reaches to 30.1 W h kg^{-1} even at value of P_d as high as 16 kW kg^{-1}. Comparison with same works [33,35], the value of E_d of 65% MnO_2/MWCNT electrode is much higher at the same value of P_d. Due to value of the current density and P_d, it could be stated that MnO_2/MWCNT electrodes are suitable materials for supercapacitors.

3.5. EIS studies

EIS technique was used for an evaluation of the electrochemical capacitance and impedance behaviors of the nanocomposite electrodes. The measurements are carried out at an applied potential of 0.5 V in 0.5 M Na_2SO_4 solutions over the frequency range 0.01–10^5 Hz. Fig. 8 shows the obtained impedance spectra data for MnO_2/MWCNT electrodes with different ratios. All of the obtained curves are similar in the form, consisting of a semicircle at a high frequency that is related to the charge transfer process at the electrode/electrolyte interface, and a tail in low frequency that is related to the diffusion process in the electrodes. EIS Curves obtained from the electrodes were analyzed by complex nonlinear least square (CNLS) fitting method on the basis of the equivalent circuit given in Fig. 8 (inset).

As shown, the equivalent circuit consists of five elements, of R_s, R_{ct}, C_{dl}, Z_W, and C_F. By definition, R_s, here, is the internal resistance includes the bulk electrolyte solution resistance, the intrinsic resistance of active material and the ionic resistance of the electrolyte at current collector/electrode interface [51]. Also, R_{ct} is the charge-transfer resistance. C_{dl} and C_F represent electrical double layer capacitance at the interface of the electrode/electrolyte and pseudocapacitance, which is accounted for the faradic reaction. Finally, Z_W is Warburg resistance that is a result of the frequency dependence of ion diffusion/transport in the electrolyte to the electrode surface [52]. The obtained values of R_s, C_{dl}, R_{ct}, Z_w and C_F were calculated from the CNLS fitting of the experimental impedance spectra and are presented in Table 1.

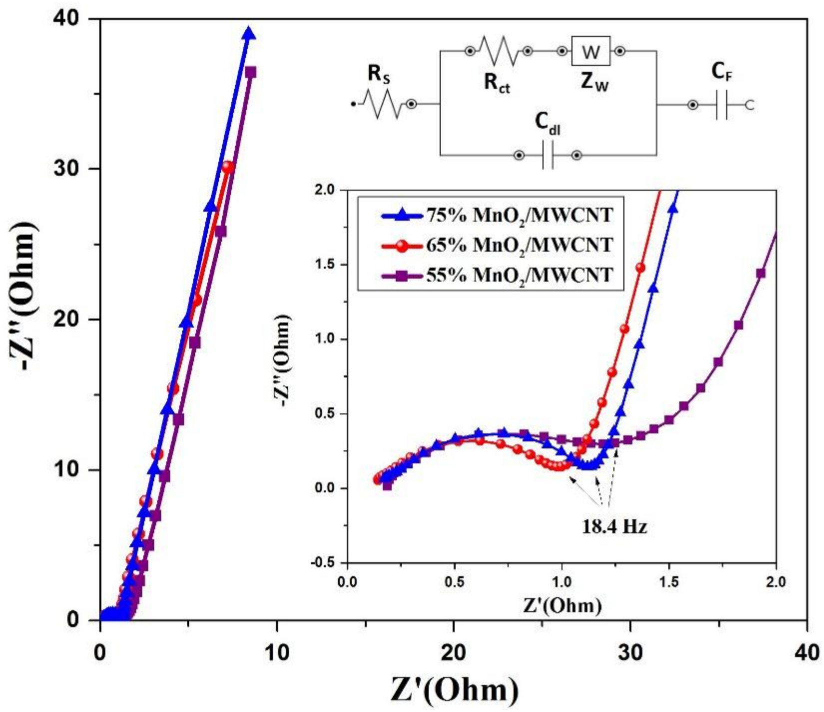

Figure 8. Nyquist plots of the impedance spectra experimentally measured on MnO$_2$/MWCNT electrodes with different ratios an applied potential of 0.5 V and the equivalent model circuit (inset).

Table 1. The calculated values of R$_s$, C$_{dl}$, R$_{ct}$, Z$_W$ and C$_F$ through CNLS fitting of the experimental impedance spectra based upon the proposed equivalent circuit.

Fitting parameters	55% MnO$_2$/MWCNT	65% MnO$_2$/MWCNT	75% MnO$_2$/MWCNT
R_s(mOhm)	211	172	201
C_{dl} (mF)	0.52	0.47	0.63
Z_W (mMho)	665	812	864
R_{ct} (mOhm)	882	690	702
C_F (mF)	435	580	545

These results are well reproducible, and the mean error of modulus is smaller than 3% that represents a good fitting of the experimental data. The R_s value is almost the same for all electrodes. A major difference is the semicircle in the high-frequency range, which corresponds to the R_{ct} caused by the faradaic reactions and C_{dl} on the grain surface. The R_{ct} of the 65% MnO$_2$/MWCNT electrode are smaller than of other nanocomposite electrodes. In the cases of 65% MnO$_2$/MWCNT electrode, such lower value of the R_{ct} is indicated of more facilitation for the electrochemical processes in the electrode interface. According to CVs and charge/discharge data, is expected the value of C_F for the 65% MnO_2/MWCNT electrode is better than the other electrodes. For the same reason, it can be seen in Table 1, the 65% MnO_2/MWCNT electrode shows better electrochemical performance than what seen for other composite electrodes. Furthermore, the MnO_2/MWCNT electrodes shows ideal Warburg resistance; where a more vertical line indicates that the electrodes are closer to an ideal capacitor [46]. Considering obtained data from the CVs and chronopotentiograms measurements, now, the EIS data confirm combination of MnO_2 and MWCNT creates a synergistic effect on the electrochemical processes.

4. CONCLUSION

In summary, MnO_2/MWCNT nanocomposites was prepared by a novel and simple method (sonochemistry method). The addition of MWCNT to a MnO_2 matrix improves conductivity by decreasing the ionic mass-transfer resistance. Consequently, an increase in both the specific power and energy of the electrode can be expected. The results show that supercapacitive performance of the MnO_2/MWCNT electrodes are better than the MnO_2 electrode. The maximum SC of the 65% MnO_2/MWCNT electrode reaches up to 394 F g^{-1} at a scan rate 2 mV s^{-1}, which is 36% higher than that of MnO_2 (289 F g^{-1}). The stability of MnO_2/MWCNT electrode was studied by FFTCCV technique in the high scan rate (200 mV s^{-1}). The FFTCCV study exhibited the SC of the MnO_2 and MnO_2/MWCNT electrodes retain approximately 82.1% and 96.8% of the initial value after 4000 cycles. The EIS and galvanostatic charge–discharge studies confirm the results of CV studies. The present synthetic strategy can be extended to other metal oxides and carbon material such as graphene, mesopores carbons. The results suggest that the fabricated MnO_2/MWCNT nanocomposite electrodes are very promising for the next generation of high performance supercapacitor electrodes.

ACKNOWLEDGEMENT
The authors are grateful to the Research Council of University of Tehran for the financial support of this work.

References

1. B. E. Conway, Electrochemical Supercapacitor-Scientific Fundamentals and Technological Applications, Kluwer, New York (1999).
2. M. Jayalakshmi and K. Balasubramanian, *Int. J. Electrochem. Sci.,* 3 (2008) 1196.
3. A. Ghosh and Y. H. Lee, *ChemSusChem,* 5 (2012) 480.
4. K. Adib, M. Rahimi-Nasrabadi, Z. Rezvani, S. M. Pourmortazavi, F. Ahmadi, H. R. Naderi and M.R. Ganjali, *J. Mater. Sci.*, (2016) in press, DOI: 10.1007/s10854-016-4329-4.
5. L. Yuan, C. Wan and L. Zhao, *Int. J. Electrochem. Sci.*, 10 (2015) 9456.
6. J. S. Shayeh, A. Ehsani, M. R. Ganjali, P. Norouzi and B. Jaleh, *Appl. Surf. Sci.*, 353 (2015) 594.
7. P. Razmjoo, B. Sabour, S. Dalvand, M. Aghazadeh and M. R. Ganjali, *J. Electrochem. Soc.* 161 (2014) D293.

8. Y. Li, S. Zhang, Q. Chen, J. Jiang, *Int. J. Electrochem.*, 10 (2015) 6199.
9. A. Barani, M. Aghazadeh, M. R. Ganjali, B. Sabour, A. A. M. Barmi and S. Dalvand, *Mater. Sci. in Semiconductor Processing*, 23 (2014) 85.
10. M. Aghazadeh, B. Sabour, M. R. Ganjali and S. Dalvand, *Appl. Surf. Sci.*, 313 (2014) 581.
11. S. Gupta, M. vanMeveren, and J. Jasinski, *Int. J. Electrochem. Sci.*, 10 (2015) 10272.
12. J. Tizfahm, M. Aghazadeh, M. G. Maragheh, M. R. Ganjali, P. Norouzi, and F. Faridbod, *Mater. Lett.*, 167 (2016) 153.
13. M. Rastgar, A. R. Zolfaghari, H. R. Mortaheb, H. Sayahi, H. R. Naderi, *J. Adv. Oxid. Technol.,* 16 (2016) 292.
14. M. Aghazadeh, M. G. Maragheh, M. R. Ganjali, P. Norouzi, D. Gharailuo and F. Faridbod, *J. Mater. Sci.: Materials in Electronics*, (2016) in press, 10.1007/s10854-016-4757-1.
15. Y. Yang and C. Huang, *J. Solid State Electrochem.,* 14 (2010) 1293.
16. S. C. Pang, M. A. Anderson and T. W. Chapman, *J. Electrochem. Soc.,* 147 (2000) 444.
17. M. Toupin, T. Brousse and D. Bélanger, *Chem. Mater.*, 16 (2004) 3184.
18. S. L. Kuo and N. L. Wu, *J. Electrochem. Soc.*, 153 (2006) A1317.
19. L. Athouel, F. Moser, R. Dugas, O. Crosnier, D. Belanger and T. Brousse, *J. Phys. Chem. C,* 112 (2008) 7270.
20. S. B. Ma, K. Y. Ahn, E. S. Lee, K. H. Oh and K. B. Kim, *Carbon*, 45 (2007) 375.
21. M. Toupin, T. Brousse and D. Belanger, *Chem. Mater.,* 14 (2002) 3946.
22. P. K. Nayak and N. Munichandraiah, *Mater. Sci. Eng. B,* 177 (2012) 849.
23. J. Yan, Z. Fan, T. Wei, W. Qian, M. Zhang and F. Wei, *Carbon,* 47 (2005) 3371.
24. Y. J. Yang, E. H. Liu, L. M. Li, Z. Z. Huang, H. J. Shen and X. X. Xiang, *J. Alloy. Compound.*, 487 (2009) 564.
25. J. Yan, Z. Fan, T. Wei, Z. Qie, S. Wang and M. Zhang, *Mater. Sci. Engin. B*, 151 (2008) 174.
26. M. Pang, G. Long, S. Jiang, Y. Ji, W. Han, B. Wang, X. Liu, Y. Xi, *Mater. Sci. Engin. B*, 194 (2015) 41.
27. X. Dong, W. Shen, J. Gu, L. Xiong, Y. Zhu and H. J. Li, *J. Phys. Chem. B,* 110 (2006) 6015.
28. S.M. Zhu, H.S. Zhou, M. Hibino, I. Honma, and M. Ichihara, *Adv. Functional Mater.,* 15 (2005) 381.
29. A. Zolfaghari, H. R. Naderi and H. R. Mortaheb, *J. Electroanal. Chem.,* 697 (2013) 60.
30. X. Xie and L. Gao, *Carbon,* 45 (2007) 2365.
31. H. Wang, C. Peng, F. Peng, H. Yu and J. Yang, *Mater. Sci. Eng. B,* 176 (2011) 1073.
32. Y. Xiao, Q. Zhang, J. Yan, T. Wei, Z. Fan and F. Wei, *J. Electroanal. Chem.*, 684 (2012) 32.
33. K. W. Nam, C. W. Lee, X. Q. Yang, B. Cho, W. S. Yoon and K. B. Kim, *J. Power Sources,* 188 (2009) 323.
34. Y. J. Kang, B. Kim, H. Chung and W. Kim, *Synthetic Metals*, 160 (2010) 2510.
35. L. Hu, W. Chen, W. Xie, N. Liu, Y. Yang, H. Wu, Y. Yao, M. Pasta, H. N. Alshareef, and Y. Cui, *Acsnano,* 5 (2011) 8904.
36. W. Yaohui, L. Hao, S. Xueliang and I. Zhitomirsky, *Scripta Materialia*, 61 (2009) 1079.
37. V. Khomenko, E. Frackowiak and F. Beguin, *Electrochim. Acta,* 50 (2005) 2499.
38. X. Qin, S. Durbach and G. T. Wu, *Carbon,* 42 (2004) 423.
39. J. S. Shayeh, A. Ehsani, A. Nikkar, P. Norouzi, M. R. Ganjali and M. Wojdyla, *New J. Chem.*, 39 (2015) 9454.
40. J. S. Shayeh, P. Norouzi, M. R. Ganjali, M. Wojdyla, K. Fic and E. Frackowiak, *RSC Advances,* 5 (2015) 84076.
41. S. Shahabi, P. Norouzi and M. R. Ganjali, *Int. J. Electrochem. Sci.*, 10 (2015) 2646.
42. P. Norouzi, B. Larijani, M. R. Ganjali and F. Faridbod, *Int. J. Electrochem. Sci.*, 9 (2014) 3130.
43. P. Norouzi, M. R. Ganjali, T. Alizadeh and P. Daneshgar, *Electroanalysis,* 18 (2006) 947.
44. P. Norouzi, M. R. Ganjali and L. Hajiaghababaei, *Anal. Lett.*, 39 (2006) 1941.
45. H. R. Naderi, P. Norouzi and M. R. Ganjali, *Appl. Surf. Sci.,* 366 (2016) 552.

46. H. R. Naderi, P. Norouzi and M. R. Ganjali, *Mater. Chem. Phys.*, 163 (2015) 38.
47. A. S. Dezfuli, M. R. Ganjali, H. R. Naderi and P. Norouzi, *RSC Advances,* 5 (2015) 46050.
48. C. C. Ji, M. W. Xu, S. J. Bao, C. J. Cai, R. Y. Wang and D. Z. Jia, *J. Solid State Electrochem.*, 17 (2013) 1357.
49. S. Devaraj and N. Munichandraiah, *J. Phys. Chem. C,* 112 (2008) 4406.
50. R.N. Reddy and R.G. Reddy, *J. Power Sources,* 132 (2004) 315.
51. H. R. Naderi, H. R. Mortaheb and A. Zolfaghari, *J. Electroanal. Chem.*, 719 (2014) 98.
52. M. D. Stoller, S. J. Park, Y. W. Zhu, J. H. An and R. S. Ruoff, *Nano Lett.,* 8 (2008) 3498.